Sustainable Food Technology

REVIEW

View Article Online
View Journal | View Issue

Cite this: *Sustainable Food Technol.*, 2024, **2**, 266

Food quality assessment using chemoresistive gas sensors: achievements and future perspectives

Seon Ju Park,†[a] Soo Min Lee,†[a] Mi-Hwa Oh,*[b] Yoon Suk Huh *[c] and Ho Won Jang *[ad]

Real-time monitoring of food freshness facilitates the supply of safe and high-quality food products to customers. Various gases, including C_2H_4, NH_3, C_3H_9N, and H_2S, can be generated during the spoilage or ripening process of food, providing insights into the state of food freshness. Chemoresistive gas sensors represent one of the reliable pathways to assess food quality due to their high sensitivity, fast response speed, and easy integration. In this paper, we review recent progress in chemoresistive gas sensors for applications in food quality monitoring. Diverse materials, such as metal oxides, carbon-based materials, transition metal dichalcogenides, and other emerging materials, have been proposed with discussions on their sensing mechanisms. This review primarily focuses on the key strategies to enhance the sensitivity and selectivity of specific food quality marker gases using the chemical properties of materials. Additionally, we address the remaining challenges hindering the practical application of chemoresistive gas sensors, such as water poisoning, power consumption, and sensor reliability, while proposing potential solutions. The chemoresistive sensor platform, encompassing functional sensing materials and data recognition systems, can pave the way for real-time food quality monitoring technology in the future.

Received 20th October 2023
Accepted 13th December 2023

DOI: 10.1039/d3fb00196b

rsc.li/susfoodtech

Sustainability spotlight

Various gases generated during the food spoilage or ripening process are reliable indicators for food freshness assessment. In this perspective, chemoresistive gas sensors are plausible candidates for real-time food quality monitoring due to their advantages such as cost effectiveness, fast response, and facile miniaturization. Developing high performance chemoresistive gas sensors and combining them with machine learning technologies can be a sustainable strategy for ensuring the consistent delivery of high quality food products to consumers. We believe this review could pave the way for sustainable possibilities in agricultural and food packaging applications.

1. Introduction

To date, with the rapid growth of the food industry and expansion of the supply chain, real-time monitoring of food freshness is demanded to ensure the safety and quality of food products. The early-stage monitoring of food spoilage not only reduces the risk of waste products but also prevents food-borne disease. Furthermore, for foods such as fruits that undergo maturation, monitoring their ripening stages enables the large-scale cultivation of high-quality products.

Food products undergo various changes over time due to microbial growth or metabolism. Traditionally, diverse techniques have been used to detect such changes and assess overall food quality. For instance, a pH indicator, like a colorimetric sensor,[1,2] can evaluate changes in food acidity caused by the production of organic acids or bases. This sensor allows real-time monitoring of food quality and can be integrated into food packaging. However, variations in temperature and illumination conditions may pose challenges in accurately determining the actual state of the product *via* visual means.[3,4] Microbial sensors, on the other hand, measure the presence of microorganisms formed during food spoilage, providing an estimation of food quality.[5,6] These sensors use fluidic devices containing antibodies that react with bacteria. While they offer real-time and large-scale measurement of microbial presence within food products, they require sophisticated equipment.

Recently, researchers have proposed an alternative method for monitoring food quality that involves detecting gases

[a]*Department of Material Science and Engineering, Research Institute of Advanced Materials, Seoul National University, Seoul 08826, Republic of Korea. E-mail: hwjang@snu.ac.kr*

[b]*National Institute of Animal Science, Rural Development Administration, Wanju 55365, Republic of Korea. E-mail: moh@korea.kr*

[c]*NanoBio High-Tech Materials Research Center, Department of Biological Engineering, Inha University, 100 Inha-ro, Incheon 22212, Republic of Korea. E-mail: yunsuk.huh@inha.ac.kr*

[d]*Advanced Institute of Convergence Technology, Seoul National University, Seoul 08826, Republic of Korea*

† These authors contributed equally to this work.

produced during the spoilage or ripening stages of food. For instance, trimethylamine (C_3H_9N, TMA) is generated during the spoilage process of fish and meats and its concentration gradually increases over time.[7] Similarly, ethylene (C_2H_4) is a plant hormone gas produced during the growth and ripening of fruits.[8] Therefore, the detection of these gases gives a reliable pathway for food freshness monitoring. In this regard, chemoresistive gas sensors can be suggested as a valuable technology for real-time food quality assessment. They take numerous advantages such as fast response speed, cost-effectiveness, and miniaturization capabilities.[9,10] To date, several results have been reported on food-generated gas detection using chemoresistive gas sensors.[11]

In this review, we will explore the fundamental operating mechanism of chemoresistive gas sensors and introduce their research trends in food quality monitoring fields. The main focus of this review is the achievement of selective detections toward target gases for real-time application, where numerous gas species coexist simultaneously. Furthermore, the challenges, potential solutions, and future perspectives of employing chemoresistive gas sensors for food quality monitoring will be discussed.

2. Chemoresistive gas sensors: overview

For real-time detection of food freshness, it is necessary to develop a sensor platform with integrated sensor arrays (Fig. 1). To achieve this, single gas sensors with high sensitivity and selectivity to various food freshness marker gases, even at low concentrations, should be evolved. In this section, we will provide a detailed review of the operating mechanism, evaluation parameters, candidate materials, and design method for chemoresistive gas sensors.

2.1 Operating mechanism of chemoresistive gas sensors

The operating mechanism of chemoresistive gas sensors has been extensively reported.[12] The general operating principle involves the injection or extraction of charge carriers within the material through redox reactions between active adsorbed oxygen species and the target gases. This mechanism is illustrated in Fig. 2.

In the ambient atmosphere, negatively charged oxygen species (O_2^-, O^-, and O^{2-}) adsorb onto the surface of the material, resulting in the formation of electron depletion layers (EDLs) in n-type materials (Fig. 2a) and hole accumulation layers (HALs) in p-type materials (Fig. 2b). Upon exposure to reducing gases such as CO, C_2H_5OH, and NH_3, these gases react with adsorbed oxygen species and inject electrons into the EDLs or HALs of the material. Therefore, the resistance of the chemoresistor decreases (n-type) or increases (p-type) (Fig. 2c and d). On the other hand, oxidizing gases such as NO_2 directly adsorb onto the surface of materials, extracting electrons and thereby expanding the EDLs or HALs. This leads to an increase (n-type) or a decrease (p-type) in the resistance of the material.

Some specific chemoresistors, especially two-dimensional (2D) nanomaterials, operate through an alternative sensing mechanism.[13] Analytic gas molecules directly interact with material and exchange charge carriers. In p-type 2D materials, oxidizing gases (NO_2) withdraw electrons, inducing a decrease in resistance. In contrast, reducing gases (CO and NH_3) inject electrons, resulting in an increase in resistance. The n-type 2D materials exhibit the opposite phenomenon of chemoresistive variations.

2.2. Evaluation parameters of chemoresistive gas sensors

The gas sensing performance can be evaluated using several parameters, including response, sensitivity, selectivity, limit of detection, response/recovery times, and stability. These parameters play a vital role in choosing the appropriate solutions for specific applications. The response (S) of the sensor (n-type) is usually defined as $R_aR_g^{-1} - 1$ when the sensor is exposed to reducing gas and as $R_gR_a^{-1} - 1$ when exposed to oxidizing gas; where R_a and R_g represent the sensor resistance in air and analyte gas, respectively. Sensitivity refers to the change in response per unit concentration of analyte gas. This can be calculated as the slope of the plot showing analyte gas response *vs.* concentrations. Another crucial parameter for determining sensing performance is selectivity. Selectivity represents the ability of a sensor to detect a target gas despite the presence of interfering gasses. Typically, it is defined as response ratio, S_T/S_I, where S_T and S_I are the sensor responses to the target gas and interfering gas, respectively.

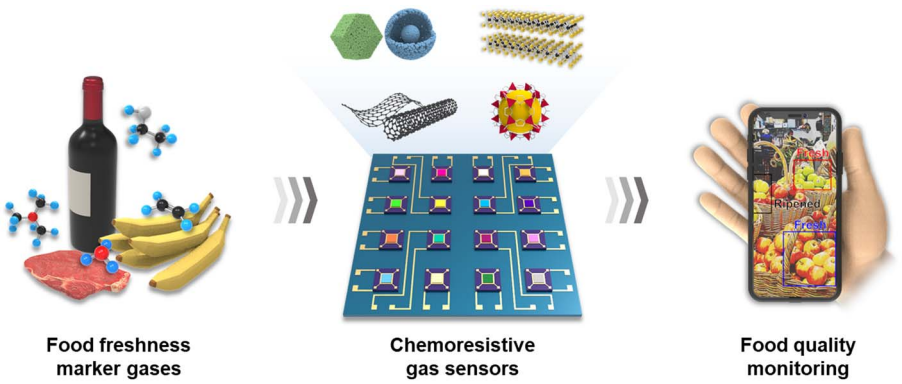

Fig. 1 Schematic diagram of chemoresistive gas sensors for food quality monitoring.

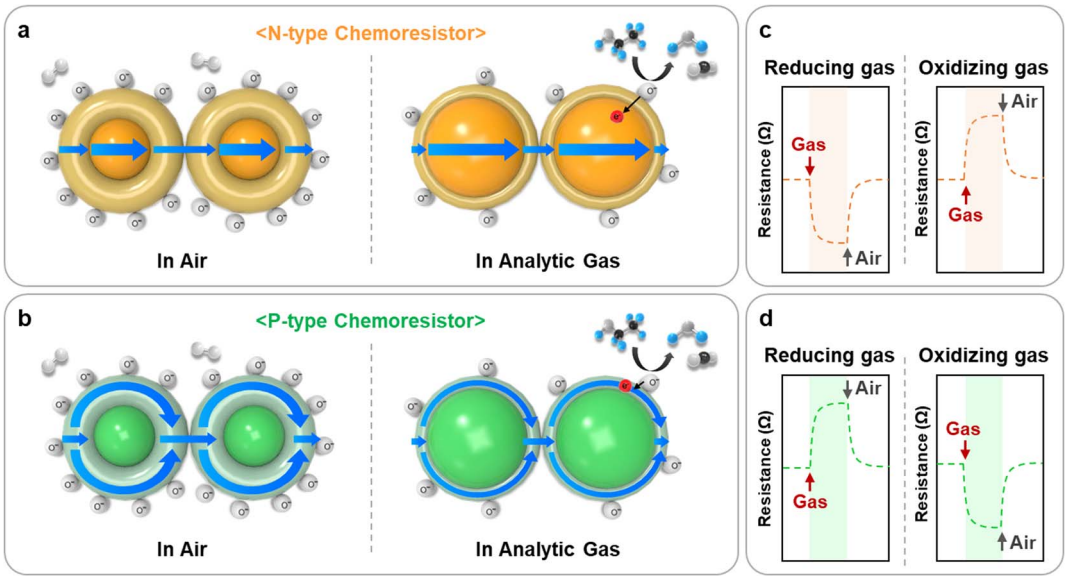

Fig. 2 Gas sensing mechanism and resistance transients of (a), (c) n-type and (b), (d) p-type chemoresistive gas sensors.

The limit of detection (LOD) is the lowest measurable concentration of analyte gases. Representative criteria for calculating the theoretical detection limit include $R_aR_g^{-1}$ >1.2 (ref. 14 and 15) and a signal-to-noise ratio >3.[16,17] Additionally, the dynamic behavior of the sensor can be evaluated by measuring the response and recovery times. The response time is the duration needed to achieve stable sensor resistance when the sensor is exposed to analyte gas. Conversely, recovery time is the time required for the sensor to return to its initial resistance in the absence of analyte gas. Typically, the time taken to reach 90% of the resistance change is referred to as the response and recovery time. The reliability of the sensor can be confirmed by measuring the repetitive sensor response over an extended period. Also, the stability of the sensor under varying humid conditions is a significant factor, and it will be discussed in detail in the following session.

2.3. Materials for chemoresistive gas sensors

The primary operation principle of chemoresistive gas sensors relies on the variations in the electrical resistance of sensing material upon exposure to the analytic gas. Various materials have been employed for chemoresistors, including metal oxide semiconductors (MOSs), carbon-based materials, and transition metal dichalcogenides (TMDs) (Table 1).

MOSs such as SnO_2, WO_3, In_2O_3, Co_3O_4, and NiO have been used as sensing materials for detecting various gases, including C_2H_5OH, NH_3, H_2S, and CO.[18–21] These MOSs possess abundant adsorbed oxygen species, which play a crucial role in inducing resistance changes and contributes to their excellent sensing performance. However, their operating temperatures are relatively high (200–500 °C), resulting in high power consumption and poor long-term stability.

From this perspective, carbon-based materials such as carbon nanotube (CNTs), graphene (Gr), and reduced graphene oxide (rGO) have been suggested as another candidate for chemoresistors owing to their flexibility, low operating temperature (RT–100 °C), and high chemical tunability.[22–27] Furthermore, TMDs such as MoS_2, WS_2, SnS_2, and $MoSe_2$ have received significant attention as sensing materials for detection of NH_3, H_2S, and NO_2.[28–31] Their 2D structures with high specific surface areas and abundant active edge sites enhance the adsorption of gas molecules, resulting in sensitive sensing performance.[32,33] The unique characteristics of 2D TMDs, such as adjustable bandgap and flexibility, provide a diverse range of sensing materials with relatively low operating temperatures (RT–250 °C).

As emerging materials, metal–organic frameworks (MOFs) are being explored for their application in chemoresistive gas sensors due to their diverse advantages such as abundant mesopores, ultrahigh specific surface area, and high catalytic activities.[34–36] Their porous structures provide high gas accessibility and abundant adsorption sites which facilitate the gas sensing reactions.[37,38] Furthermore, some specific 2D structured conductive MOFs can be operated even at room temperature

Table 1 Material type, materials, typical operating temperature, and major target gases of chemoresistive gas sensors

Material type	Materials	Operating temp.	Target gases	Ref.
Metal oxide	SnO_2, WO_3, In_2O_3, TiO_2, Fe_2O_3, NiO, Co_3O_4	200–500 °C	Most gases	14, 18–20, 50, 52
Carbon-based materials	CNTs, Gr, rGO	RT–100 °C	NO_2, NH_3	23–25
TMDs	MoS_2, SnS_2, WS_2, In_2S_3, MoSe	RT–250 °C	NO_2, H_2S, NH_3	28–30
MOFs	$Cu_3(HHTP)_2$, $Ni_3(HITP)_2$, $Co_3(HITP)_2$	RT–150 °C	NO_2, NH_3, H_2S	39, 40
MXenes	$Ti_3C_2T_x$, V_2CT_x, $V_4C_3T_x$	RT–150 °C	C_2H_5OH, CH_3COCH_3, H_2, CH_4	43–45

(RT) with high gas selectivity.[39,40] Additionally, other materials such as covalent organic frameworks (COFs),[41,42] MXene,[43–45] or their hybrids[46–49] are garnering intense attention as potential candidates for gas sensing applications.

2.4. Material design for chemoresistive gas sensors

Nanostructured materials with abundant active sites and high gas accessibility facilitate rapid and effective sensing reactions. The analytic gas permeates sensing materials through their pores and reacts with adsorbed oxygen species. Therefore, it is crucial to design the configuration of nanostructures such as size, porosity, and thickness to enhance gas sensing performance. For example, our coworkers prepared highly gas accessible Fe_2O_3 nanotube arrays *via* the glancing angle deposition (GAD) process.[50] The vertically aligned Fe_2O_3 nanotube arrays exhibited improved acetone response compared to dense planar Fe_2O_3 thin film. Notably, the Fe_2O_3 nanotube arrays showed a rapid response time of less than 3 s. This can be attributed to their large specific surface area and the presence of nanosized narrow necks.[16] Jo *et al.* reported hierarchical Co_3O_4 hollow nanocages prepared by MOF template.[51] The shell of hollow nanocages was composed of thin nanosheet building blocks, facilitating the gas permeation within the nanostructure. The response to xylene increased as both the size and shell thickness of the nanocages decreased. However, when the size of nanocages became extremely small, the xylene response decreased significantly due to the reduced gas accessibility caused by the particle agglomeration. These findings suggest that optimal particle size and thickness should be considered when designing gas sensing materials. Numerous studies have focused on improving gas sensing ability *via* designing nanostructures such as nanowires, nanosheets, hollow, hierarchical, and porous films.[52–55]

Forming a heterostructure or heterojunction between sensing materials and catalysts such as metal and metal oxide can be a viable strategy to control sensing characteristics. This approach allows the modulation of the thickness of EDLs/HALs, tuning of catalytic activity, and the adjustment of chemical affinity to specific gases.[56,57] First, the enlargement in EDLs/HALs increases sensor response due to the higher variation in charge carrier concentration upon exposure to analyte gases. Therefore, metal and metal oxide catalysts with high work functions have been loaded/doped onto sensing materials to achieve high gas response. For instance, our coworkers decorated Au nanoparticles (NPs) on WO_3 to increase response to ethanol and NO_2 by decreasing the background charge carrier concentration of WO_3.[58] Likewise, we also fabricated the Fe_2O_3 loaded NiO nanorods *via* GAD which exhibited ultrasensitive toluene sensing properties by forming a p–n junction.[59] Second, the incorporation of additives with sensing materials can increase the number of active sites, thereby contributing to enhanced catalytic activity. Zhou *et al.* reported Rh-doped SnO_2 as a highly selective acetone sensor.[60] The Rh doping elevated the number of adsorbed oxygens, leading to a high acetone response. Also, Lee *et al.* fabricated a highly sensitive volatile organic compounds (VOCs) sensor by loading Au NPs onto the In_2O_3 inversed opal thin films.[61] The Au NPs effectively promoted oxygen adsorption, resulting in increased VOCs response. Lastly, additives showing high chemical affinity to specific gases can be employed to enhance gas sensing properties. For example, Choi *et al.* reported the CuO-loaded SnO_2 hollow spheres as an ultrasensitive H_2S gas sensor.[62] Compared to the pristine SnO_2, the CuO-loaded SnO_2 showed a 7.1 times higher response to H_2S. This can be attributed to the high chemical affinity of CuO toward H_2S, which converts CuO into CuS upon exposure to H_2S, resulting in a significant decrease in sensor resistance.[63] Also, loading Pd and PdO can increase H_2 response, as Pd triggers the H_2 spill-over effect; which decompose H_2 molecules into H atoms. For instance, Zhou *et al.* fabricated a highly sensitive and selective H_2 gas sensor by loading Pd NPs on $W_{18}O_{49}$.[64] By loading Pd NPs on $W_{18}O_{49}$, the response to H_2 increased preferentially. Also, Kim *et al.* reported a PdO-functionalized SnO_2 as a selective H_2 sensor.[65] Compared to the pristine SnO_2, the PdO-functionalized SnO_2 exhibited a 6.4 times higher response to H_2, attributable to the Pd-induced spillover effect. Overall, forming appropriate heterojunctions with sensing materials and additives can effectively enhance sensitivity and selectivity.

Functional overlayers, when deposited onto the sensing layer, possess the capability to enhance sensitivity and selectivity toward target gases. One approach involves employing a physical filtering method, utilizing the difference in molecular sizes of gases to selectively detect small-sized gases. For instance, Jo *et al.* suggested a selective formaldehyde sensor using a ZIF-7/PEBA mixed matrix membrane (MMM) coated TiO_2 sensor.[14] The pristine TiO_2 sensor showed a high response to both ethanol and formaldehyde. However, upon applying the MMM coating on the sensing layer, larger ethanol molecules were filtered out, allowing only smaller formaldehyde molecules to penetrate the sensing layer. As a result, this sensor exhibited remarkable selectivity towards formaldehyde. Alternatively, catalytic filtering layers can be applied, considering the reforming/oxidation reactions of the analyte gases. Moon *et al.* designed a Rh–TiO_2 overlaid SnO_2 sensor that selectively detected benzene over xylene and toluene.[66] The catalytic Rh–TiO_2 layer facilitated the conversion of stable benzene into reactive species (*e.g.*, aldehydes), while the interfering gases were completely oxidized (*e.g.*, CO_2 and H_2O). As demonstrated in the previous reports, the application of overlayers with physical or chemical filtering abilities can enhance the selectivity and sensitivity of chemoresistive gas sensors.

3. Chemoresistive gas sensors for food quality monitoring

Chemoresistive gas sensors are currently employed in various fields such as breath analysis, environmental, and industrial applications.[67,68] In particular, the detection of specific gases generated during the process of food spoilage, fermentation, and ripening, can provide information about the freshness stage of food items. The number of publications and citations related to this application have been significantly increased and

accounted for a large proportion compared to other fields (Fig. 3) In this section, we will focus on the development trends in chemoresistive gas sensors for detecting various food freshness marker gases and their underlying mechanisms. Table 2 provides the summary of various chemoresistive gas sensors to detect food quality marker gases.

3.1. Ethylene (C_2H_4) sensors

Ethylene (C_2H_4) is a plant hormone gas that evolves during ripening, and it has numerous effects on the growth, senescence, seed germination, ripening, browning, and softening of fruits and vegetables.[103,104] As fruits ripen, the emitted concentration of ethylene increases, accelerating the ripening process and ultimately leading to fruit spoilage. Thus, detecting ethylene in a sensitive and selective manner can be a useful strategy to determine the freshness of fruits and vegetables.

In general, most oxide semiconductors generally exhibit low response and selectivity to ethylene, as it is the simplest alkene with non-polarity and strong bonds. To overcome this limitation, pretreatment of gases such as the chemical oxidation of interference gases into less reactive or non-reactive species (*e.g.*, CO_2 and H_2O) and the ethylene reforming reaction into more reactive intermediates(*e.g.*, aldehydes) have been suggested. Jeong *et al.* reported a sensitive and selective ethylene sensor based on a Cr_2O_3–SnO_2 bilayer consisting of hollow SnO_2 spheres as a sensing layer and a nanoscale catalytic Cr_2O_3 overlayer (Fig. 4a).[69] The SnO_2 sensing layer was prepared using the screen-printing method and the catalytic Cr_2O_3 overlayer (~300 nm) was coated *via* electron-beam evaporation. The Cr_2O_3–SnO_2 sensor exhibited a significant increase in ethylene selectivity after coating the Cr_2O_3 layer ($S_{ethylene}/S_I$ >3.3 to 2.5 ppm analytic gases at 375 °C), which was 8.0 times higher than that of the pristine SnO_2. The underlying mechanisms of these results can be explained as the chemical filtration of Cr_2O_3 which induces the catalytic oxidation of more reactive interfering gases into non- or less-reactive species (*e.g.*, CO_2 and H_2O) while maintaining the response to relatively stable ethylene. They further evaluated the potential of the Cr_2O_3–SnO_2 sensor for fruit quality monitoring applications by investigating the time-dependent changes in the sensor response during fruit ripening. Moon *et al.* fabricated the Pd–V_2O_5–TiO_2 yolk–shell coated In_2O_3 bilayer sensor for ethylene detection (Fig. 4b).[70] They used the Pd–V_2O_5–TiO_2 yolk–shell overlayer as a heterogeneous Wacker oxidation catalyst, which reforms less reactive ethylene into highly reactive acetaldehyde. This reforming reaction improved the response to ethylene, as acetaldehyde is a well-known reactive species. The conversion of ethylene to acetaldehyde through the Pd–V_2O_5–TiO_2 overlayer was confirmed using proton transfer quadrupole mass spectroscopy. The Pd–V_2O_5–TiO_2/In_2O_3 bilayer sensor exhibited 15.5 times higher sensitivity to ethylene ($R_aR_g^{-1} - 1 = 18.6$ to 5 ppm at 300 °C) compared to that of the pristine In_2O_3 sensor and 41.4 times higher selectivity owing to the catalytic filtering of Pd–V_2O_5–TiO_2.

Ethylene sensors using carbon-based materials have been also reported. Esser *et al.* prepared a single-wall carbon nanotube with Cu(I) complexes (1-SWNT) for an ethylene sensor.[71] They proposed the Cu(I) complex as an ethylene receptor, as Cu(I) has been found to be a cofactor of ethylene receptor (ETR1) in plants during the ripening process (Fig. 4c). The 1-SWNT showed significantly enhanced ethylene response and selectivity compared to those of the pristine SWNT. They further confirmed the feasibility of 1-SWNT sensor to real-time fruit freshness quality monitoring by measuring the time-dependent changes in the sensor response upon exposure to various fruits (banana, avocado, apple, pear, and orange).

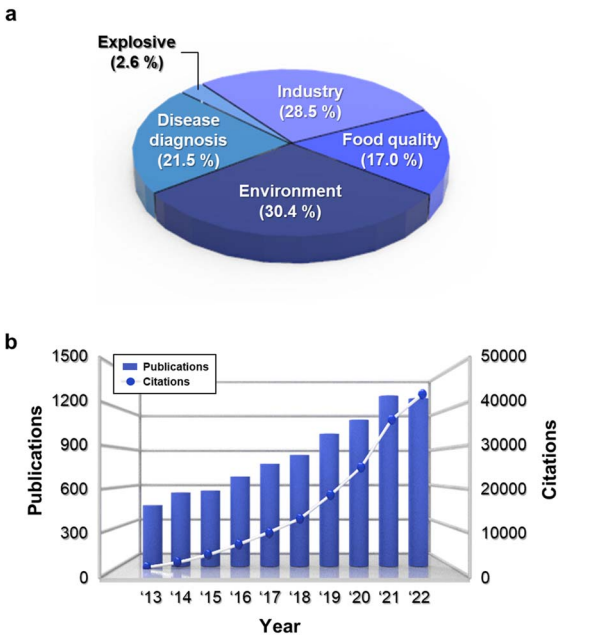

Fig. 3 (a) Diverse applications of chemoresistive gas sensors reported in the literature, (b) the number of publications and citations on chemoresistive sensors for food quality monitoring. The data was collected using Web of Science – Web of Science Core Collection Search: keywords of (gas sens* or chemiresis* or chemoresis*) and environment* or industry* or breath* or health* or food or explosive* were used.

3.2. Ammonia (NH_3) sensors

Ammonia (NH_3) is a toxic and harmful gas emitted from fish and meat, resulting from the bacterial degradation of protein in foods.[105] Certain types of fish, including fermented skates, possess a strong ammonia odor, which is intensified as spoilage advances.[106] Consequently, the detection of NH_3 can serve as a reliable indicator of the freshness or spoilage state of fish and meat.

Several research studies were conducted to detect NH_3 at low concentration levels in a highly selective and sensitive manner. Especially, sulfide-based TMD materials, including MoS_2, exhibited a high sensitivity to NH_3 due to the their chemical affinity.[74,75] Our group reported a highly selective NH_3 sensor with low operating power (19 mW) by integrating the MoS_2 nanoflakes onto a MEMS (micro-electromechanical systems) platform (Fig. 5a).[76] The pristine MoS_2 exhibited a high response and selectivity to NH_3 ($R_aR_g^{-1} - 1 = 4.7$, S_{NH_3}/S_I >8.0 to 50 ppm at 150 °C). It is attributable to the strong binding energy of the MoS_2 edge site to NH_3, which was confirmed by density

Table 2 Summary of chemoresistive gas sensors for food quality marker gases (response was defined as $R_aR_g^{-1}$, $R_aR_g^{-1} - 1$, $R_gR_a^{-1}$, $R_gR_a^{-1} - 1$, $I_aI_g^{-1}$, $I_aI_g^{-1} - 1$, $I_gI_a^{-1}$, or $I_gI_a^{-1} - 1$)

Gas	Materials	Conc. [ppm]	Response	Operating temp. [°C]	LOD [ppb]	Food	Ref.
C_2H_4	Cr_2O_3–SnO_2 hollow spheres	2.5	16.8	350	24	Banana	69
	Pd–V_2O_5–TiO_2/In_2O_3 bilayer	1	18.6	325	7.3	Banana	70
	Cu-SWNT	50	1.7	RT	—	Banana, avocado, apple, pear, orange	71
	Pd–SnO_2 nanoparticle	100	11.1	250	50	Banana, lemon, apple, pear	72
	ZnO nanosheet	200	6.4	500	1.0×10^4	Banana	73
NH_3	WS_2 thin film	0.2	2.1%	30	100	—	74
	MoS_2 thin film	30	0.1%	30	300	—	75
	MoS_2 flakes	50	6.58	150	—	Fish (stingray)	76
	PTS-doped PANI	5	2.25	30	—	Fish, pork, chicken	77
	CuBr film	5	30	RT	0.2	—	78
	Fluorinated GO	500	121%	RT	6.1	—	25
	TiO_2/MXene	30	41.0%	RT (UV)	0.2	Fish, pork, shrimp	79
	CNT/metalloporphyrin	20	4.4%	RT	500	Cod, salmon, pork, chicken	80
C_3H_9N	WO_3 hollow sphere	5	56.9	450	11.8	—	81
	α-MoO_3 nanorod	200	413	RT	1000	—	82
	Pr-doped $Ce_4W_9O_{33}$	20	20.1	350	—	—	83
	MoO_3 nanoplate	5	374.7	300	45	—	84
	Co_3O_4@ZnO hollow cage	33	41	250	130	—	85
	Au–Cr_2O_3 yolk shell	5	200.9	225	4.3	—	86
	5,5″-Di(naphthalen-1-yl)-2,2′:5′,2″-terthiophene (NA-3T-NA)	2.1×10^5	4.1	RT	2.2×10^4	Fish, pork, chicken	87
H_2S	Ordered mesoporous WO_3	50	269	250	—	—	88
	Bi_2S_3/SnS_2 nanoparticle	0.5	12.3	RT	—	—	89
	CdS-ATP nanowire	10	9.99%	RT (visible light)	0.1	—	90
	Ag-doped graphene	0.5	37%	RT	100	—	91
	MIL-88B (Fe) nanoparticle	100	1056	RT	170	—	92
	$Ni_3(HHTP)_2$ thin film	5	20.85	RT	3	—	93
	$SnSe_2$/WO_3 nanoparticle	10	33.8%	RT	28	Egg	94
	NiO-doped CuO composite	1	106%	180	1	Fish, pork	95
	Macroporous ZnO@ZIF-8/Pt	5.5	118	310	40	Fish, shrimp	96
	Inverse opal $ZnCoO_x$@BM-ZIF	5	260	180	70	Chicken	97
CH_3CHO	Al-doped ZnO	0.4	50.6	200	—	—	98
	Hierarchical SnO_2 nanoparticle	100	178.3	243	500	—	99
CH_3COOH	Hierarchical SnO_2 nanoflowers	100	47.7	260	—	—	100
	Mesoporous CuO nanoparticle	100	27.2	200	—	—	101
	Peptide encapsulated SWCNTs	0.4×10^4	21%	RT	—	Wine	102

functional theory (DFT) calculations. The sensing performance of this sensor was further examined under exposure to a fresh skate for 5 days at RT. At fresh state, the sensor showed a negligible response, however, after 5 days, the response reached 26.5. The sensor response exhibited a linear correlation with fermentation time, suggesting that this sensor has the potential as a reliable food quality monitoring application.

Furthermore, NH_3 was selectively detected using conducting polymer or ionic conductor thin films.[107] Ma *et al.* reported a highly sensitive and wireless meat spoilage sensor using polyaniline (PANI) based material (Fig. 5b).[77] They doped iron(III) *p*-toluene sulfonate hexahydrate (PTS) in PANI to enhance the sensing performance, and this sensor exhibited a high response ($\Delta RR_0^{-1} = 2.25$) toward 5 ppm NH_3. Furthermore, the author measured the sensor response to various meat products (pork, beef, chicken, and fish) at 30 °C for 20 h. The sensor showed a high response ($R_gR_a^{-1} - 1 = 1.0$–5.0) which varied with the type of meat, due to the different protein levels. Güntner *et al.* reported a rapid and selective NH_3 sensor using a porous CuBr film (Fig. 5c).[78] The sensor discriminated NH_3 by forming a stable amine complex ($Cu(NH_3)^{2+}$), resulting in a significant decrease in conductivity. The porous film structure (porosity = 78%) facilitated the efficient NH_3 diffusion and interaction with the CuBr surface. Therefore, this sensor exhibited rapid response speed (2.2 min), high selectivity ($S_{NH_3}/S_I > 30$), and low detection limit (LOD = 210 ppt with the criterion of signal-to-ratio >3) at RT and highly humid atmosphere (90% RH; relative humidity). Additionally, there are several reports on the development of highly selective, flexible, and RT operating NH_3 sensors using emerging materials such as graphene, carbon nanotube, and Mxene.[25,79,80]

3.4. Trimethylamine (C_3H_9N) sensors

Most marine mammal products contain trimethylamine oxide (TMAO), which is converted into TMA gas through the metabolism process of anaerobic bacteria.[108,109] Moreover, various

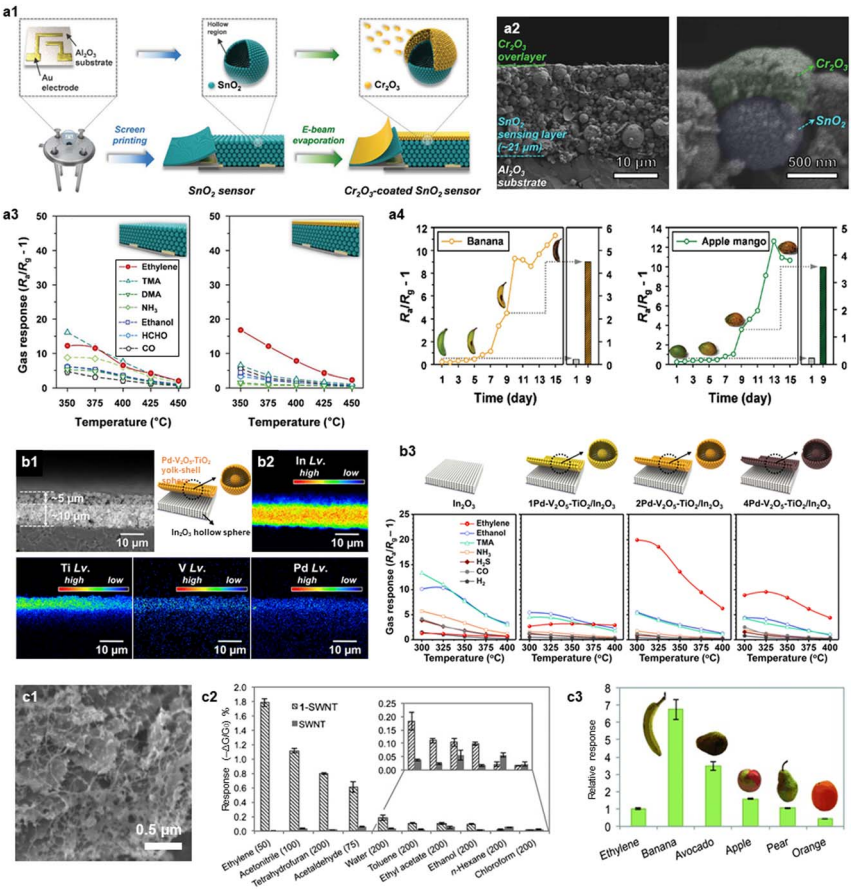

Fig. 4 Ethylene sensors. (a1) Illustration of Cr_2O_3–SnO_2bilayer sensor fabrication process, (a2) cross-section scanning electron microscopy (SEM) images of Cr_2O_3–SnO_2, (a3) gas sensing characteristics of the pristine SnO_2 sensor and the Cr_2O_3–SnO_2 bilayer sensor at the temperature range of 350–450 °C (concentration: 2.5 ppm), (a4) gas sensing properties of the Cr_2O_3–SnO_2 bilayer sensor to banana and apple mango. Reproduced with permission from ref. 69 Copyright 2019, Wiley. (b1) Cross-sectional backscattered image of Pd–V_2O_5–TiO_2/In_2O_3 bilayer sensor, (b2) electron probe micro analysis (EPMA) elemental (In, Ti, V and Pd) images of bilayer, (b3) gas sensing properties of the pristine In_2O_3 sensor and the *m*Pd–V_2O_5–TiO_2/In_2O_3 ($m = 1, 2, 4$) bilayer sensor. Reproduced with permission from ref. 70 Copyright 2023, The Royal Society of Chemistry. (c1) SEM image of 1-SWNT, (c2) gas response of the 1-SWNT and the SWNT sensor to various analyte gases at RT (concentration: 50 ppm), (c3) relative response of the 1-SWNT sensor to 100 g of different fruit to 20 ppm of ethylene. Reproduced with permission from ref. 71 Copyright 2012, Wiley.

volatile basic nitrogen gases, including TMA, are generated during the deterioration of meat.[110,111] The concentration of TMA increases as fishery products or meat products undergo spoilage, therefore, it can serve as a criterion for assessing the freshness of seafood and meat products.[112,113] For example, reported literature suggested a correlation between fish freshness and TMA concentration (fresh: 110 ppm, early corrosion: 10–50 ppm, rotting: >60 ppm).[114]

TMA is a representative amine gas that exhibits a high chemical affinity to oxides with a highly acidic surface. Cho *et al.* prepared a high-performance TMA sensor using WO_3 hollow spheres (Fig. 6a).[81] This sensor showed a high gas response ($R_aR_g^{-1} = 56.9$ at 450 °C) to 5 ppm TMA and a high selectivity ($S_{TMA}/S_I > 1.7$) over other interfering gases. Additionally, Srinivasan *et al.* proposed a MoO_3 nanorod gas sensor with high response to 200 ppm TMA ($R_aR_g^{-1} = 413$ at 30 °C; Fig. 6b).[82] This sensor also showed excellent sensing performance to other amine gases ($R_a/R_g^{-1} = 63$ and 39 for dimethylamine and monomethylamine, respectively.) Considering that both WO_3 and MoO_3 have relatively high surface acidity,[115] utilizing the acid–base interaction can be served as a promising pathway for a high-performance TMA sensor.[83,84]

Furthermore, considering that TMA has a large molecular size, increasing the adsorption of oxygen species by adding an oxidative catalyst and designing nanostructures are the effective strategies to enhance the TMA sensing ability. Yan *et al.* reported a MEMS based TMA sensor using a Co_3O_4@ZnO hollow cage synthesized with a MOF template (Fig. 6c).[85] The Co_3O_4@ZnO hollow cage exhibited enhanced TMA sensing performance ($I_gI_a^{-1} - 1 = 41$ to 33 ppm) compared to that of the bare ZnO ($I_gI_a^{-1} - 1 = 20$). The hollow cage structure with large surface area (48.4 $m^2\ g^{-1}$) and high porosity provided excellent gas accessibility and abundant active sites for oxygen species to adsorb, resulting in a high gas response. Also, the formation of p(Co_3O_4)–n(ZnO) junction increased the thickness of EDLs, inducing the higher variation in sensor resistance upon

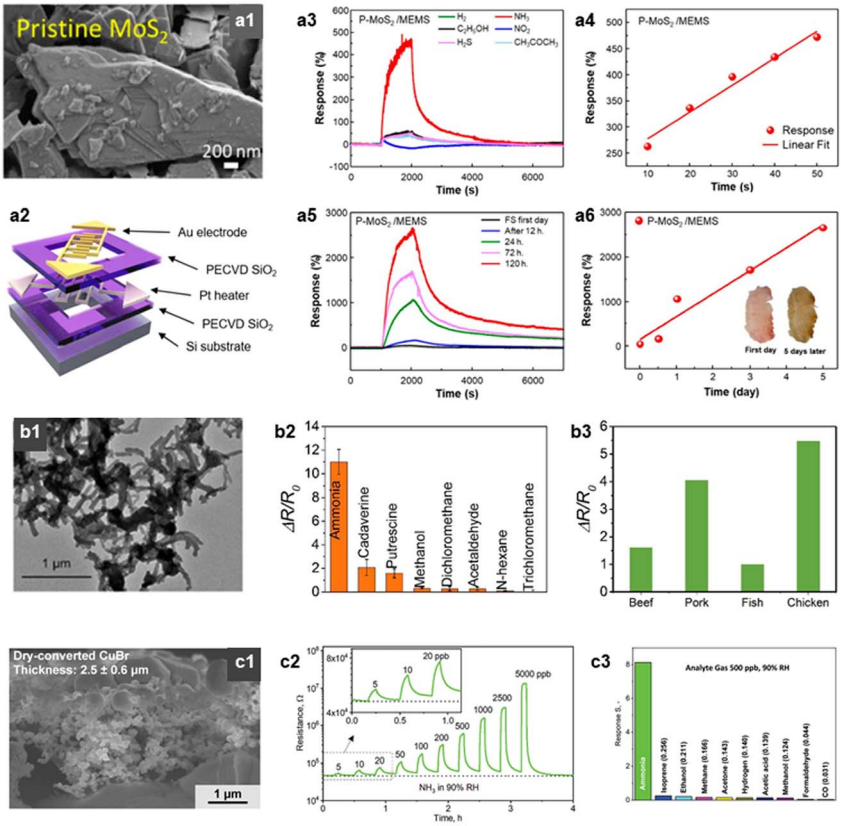

Fig. 5 NH_3 sensors. (a1) SEM image of MoS_2 nanoflakes, (a2) schematic illustration of MEMS sensor platform (operating power = 19 mW), (a3) sensor response transients of MoS_2-MEMS gas sensor to various analytic gases (concentration: 50 ppm), (a4) MoS_2-MEMS sensor response to various concentrations of NH_3 (concentration: 10–50 ppm), (a5 and a6) MoS_2-MEMS sensor response after exposure to skate depending on the fermentation time. Reproduced with permission.[74] Copyright 2023, American Chemical Society. (b1) Transmission electron microscope (TEM) image of PTS-PANI, gas responses (ΔRR_0^{-1}) of PTS-PANI sensor to (b2) various analytic gases and (b3) four kinds of raw meats (beef, pork, fish, and chicken). Reproduced with permission.[75] Copyright 2018, American Chemical Society. (c1) Cross-sectional SEM image of CuBr films, (c2) resistance change transient of CuBr gas sensor upon exposure to various concentration of NH_3 (concentration: 5–5000 ppb, RT, 90% RH), (c3) response ($R_gR_a^{-1} - 1$) of CuBr sensor to various analytic gases (concentration: 500 ppb). Reproduced with permission.[76] Copyright 2020, Wiley.

exposure to TMA. Kim *et al.* prepared an Au-loaded Cr_2O_3 yolk–shell nanostructure *via* spray pyrolysis for its use as a TMA sensor (Fig. 6d).[86] This sensor exhibited a high gas response ($R_gR_a^{-1} = 200.9$) and selectivity ($S_{TMA}/S_I > 2.1$) to 5 ppm of TMA at 250 °C. Furthermore, the calculated LOD (using $R_gR_a^{-1} > 1.2$ as a criterion) was as low as 4.3 ppb, indicating the potential use of this sensor for seafood freshness assessment. The synergistic combination of the highly gas accessible nanostructure and catalytic promotion effect of Au nanoparticles results in the superior TMA sensing performance.

3.5. Hydrogen sulfide (H_2S) sensors

Hydrogen sulfide (H_2S) is a colorless, flammable, and corrosive gas with the distinctive smell of rotten eggs. H_2S is easily produced during meat spoilage, resulting from the decomposition of sulfur-containing amino acids.[116–118] Hence, detecting H_2S can be a useful strategy to monitor meat freshness quality.

Various H_2S sensors are suggested using MOSs and TMDs. For instance, Li *et al.* prepared a well-ordered mesoporous WO_3 using the template-carbonization method for the H_2S sensor (Fig. 7a).[88] The high mesoporosity and surface area of WO_3 resulted in a high H_2S response ($R_aR_g^{-1} = 269$ to 50 ppm at 250 °C) and selectivity ($S_{H_2S}/S_I > 6$). Also, Wang *et al.* synthesized the Bi_2S_3/SnS_2 heterostructure *via* a solvothermal method and evaluated its sensing properties at RT.[89] The Bi_2S_3/SnS_2 sensor exhibited a high H_2S sensitivity ($R_aR_g^{-1} = 12.3$ to 0.5 ppm) and selectivity ($S_{H_2S}/S_I > 3.0$), attributable to the enlargement of EDLs and increased active sites after forming the heterojunctions. The CdS-based metal chalcogenide nanowire has been also reported by Jin *et al.* to detect H_2S sensitively.[90] The author functionalized the surface of CdS nanowires with an amino group (ATP = 4-aminothiophenol), as the amino group can selectively interact with H_2S *via* hydrogen bonding (Fig. 7b). The ATP functionalized CdS (Cd-ATP) nanowire showed an excellent response ($R_aR_g^{-1} = 9.99$ to 10 ppm), selectivity, and response/recovery time to H_2S under visible light irradiation at RT. Considering those reports, H_2S can be effectively detected by designing highly, gas accessible structures with abundant active sites.

Recently, carbon-based materials and MOF have garnered interest as emerging sensing materials. For instance, Ovsianytskyi *et al.* reported an Ag-doped Gr sensor, fabricated *via* the wet chemical method and measured its sensing properties toward

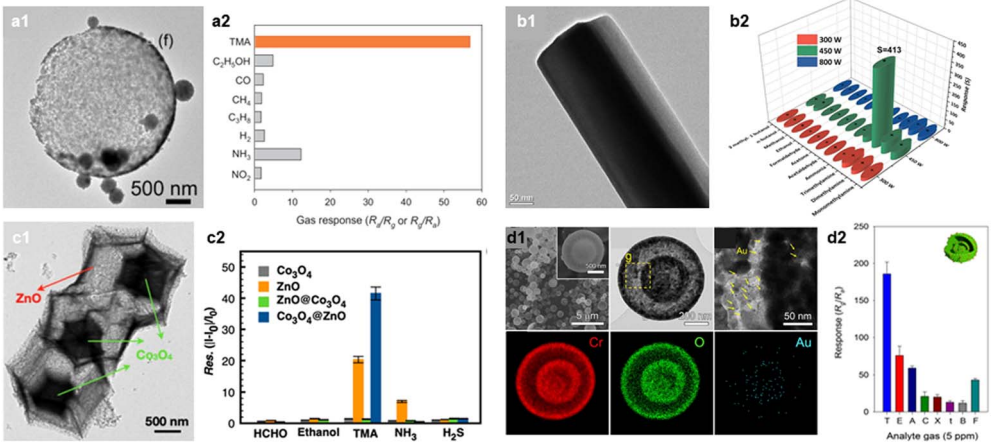

Fig. 6 TMA sensors. (a1) SEM image of WO_3 hollow spheres, (a2) gas response ($R_aR_g^{-1}$) of WO_3 hollow sphere sensor to various analytic gases (concentration: 5 ppm). Reproduced with permission.[81] Copyright 2020, Elsevier. (b1) TEM image of α-MoO_3 nanorod, (b2) gas response ($R_aR_g^{-1}$) of α-MoO_3 nanorod sensor to various gases at RT. Reproduced with permission (concentration: 200 ppm).[82] Copyright 2021, Elsevier. (c1) TEM image of Co_3O_4@ZnO nanocage, (c2) gas response ($I I_0^{-1} - 1$) of Co_3O_4@ZnO sensor to various analytic gases at 250 °C (concentration: 100 ppm). Reproduced with permission.[85] Copyright 2021, American Chemical Society. (d1) SEM, TEM, and EDS elemental mapping images of Au–Cr_2O_3 yolk–shell spheres, (d2) gas response ($R_gR_a^{-1}$) of Au–Cr_2O_3 yolk–shell gas sensor to various analytic gases at 225 °C (concentration: 5 ppm). Reproduced with permission.[86] Copyright 2017, Elsevier.

H_2S.[91] The high chemical affinity of Ag to H_2S enhanced the response and selectivity of Ag-doped Gr sensor compared to those of the pristine Gr sensor. Moreover, Wang *et al.* prepared a H_2S sensor using Fe-based MIL-88B, synthesized by a solvothermal method (Fig. 7c).[92] They controlled the pore size of MIL-88B by optimizing the solvent. An increase in the pore size of MIL-88B improved the H_2S sensitivity ($I_gI_a^{-1} - 1 = 10.56$ to 100 ppm at RT) and selectivity compared to those of the MIL-88B with smaller

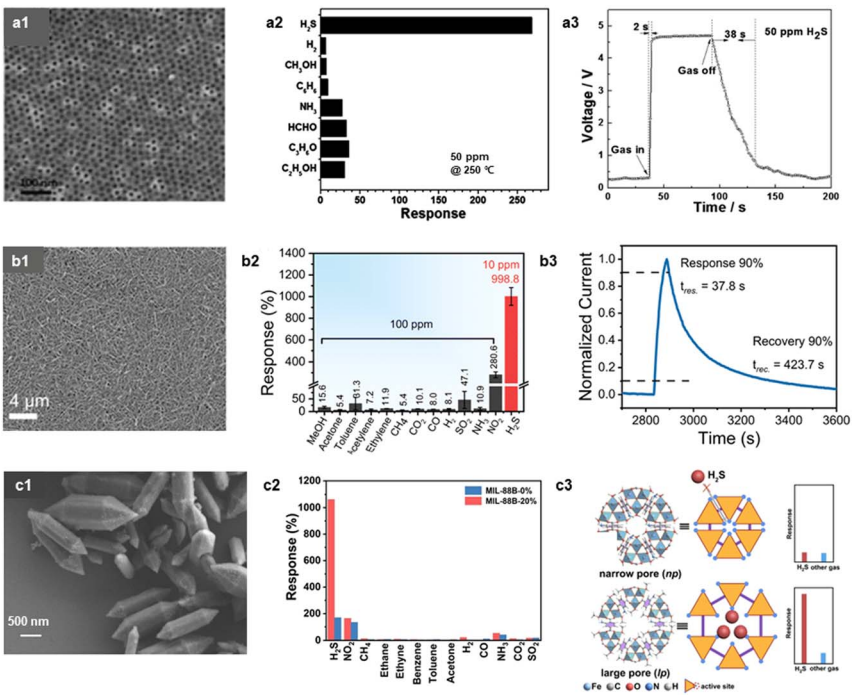

Fig. 7 H_2S sensors. (a1) SEM image of the ordered mesoporous WO_3, (a2) gas response ($R_aR_g^{-1}$) of the ordered mesoporous WO_3 to various analyte gases at 250 °C (concentration: 50 ppm), (a3) the response and recovery curve of the ordered mesoporous WO_3 to 50 ppm of H_2S at 250 °C. Reproduced with permission.[88] Copyright 2014, Wiley. (b1) SEM image of the Cd-ATP nanowires, (b2) gas response ($R_aR_g^{-1}$) of the Cd-ATP sensor to various analyte gases under visible light at RT, (b3) response and recovery curve of the Cd-ATP nanowire sensor to 100 ppm H_2S. Reproduced with permission.[90] Copyright 2023, The Royal Society of Chemistry. (c1) SEM image of the MIL-88B-20%, (c2) gas response ($I I_0^{-1} - 1$) of the MIL-88B-0% and the MIL-88B-20% to different analyte gases at RT (concentration: 100 ppm), (c3) illustration of pore-sized dependent gas sensing properties. Reproduced with permission.[92] Copyright 2023, Wiley.

pores. This enhancement is attributed to the increased surface area and improved gas accessibility to the inner Fe active sites, which was corroborated using Brunauer–Emmett–Teller (BET) analysis and DFT calculation. In addition, Lee *et al.* reported a thin-film-structured $Ni_3(HITP)_2$, a conducting MOF, which exhibited excellent H_2S sensitivity (ΔRR_a^{-1} = 20.85 to 5 ppm at RT).[93] The author suggested that the 1D pore system achieved by the planar metal–ligand complex and the oriented nature of $Ni_3(HITP)_2$ promoted the binding and redox reaction to H_2S.

3.6. Others

In addition to C_2H_4, TMA, NH_3, and H_2S, VOCs can also serve as food spoilage markers for real-time monitoring. For example, acetaldehyde (CH_3CHO), a well-known byproduct of alcohol breakdowns, is produced during the spoilage of chicken, coffee, and dairy products, including milk.[119–121] Hagedorn *et al.* proposed an Al-doped ZnO for the highly sensitive detection of acetaldehyde.[98] By doping Al on ZnO, the amount of adsorbed oxygen species on the surface of ZnO increased significantly, resulting in an extremely high acetaldehyde response at low temperature ($R_aR_g^{-1}$ = 356 to 5 ppm at 210 °C). Additionally, Li *et al.* fabricated the hierarchical butterfly-like SnO_2 nanosheets *via* a hydrothermal method to detect acetaldehyde.[99] The proposed SnO_2 nanosheets possessed a highly porous structure with a high specific surface area and abundant active sites, attributable to a selective acetaldehyde sensing property ($S_{acetaldehyde}/S_I > 4.4$).

Furthermore, acetic acid (CH_3COOH) is produced during the alcoholic fermentation of wine, making it a useful indicator for assessing wine freshness.[122,123] Jin *et al.* reported an acetic acid sensor using three-dimensional hierarchical flower-like SnO_2 synthesized by a template-free hydrothermal method.[100] The flower-like SnO_2 exhibited a high response to acetic acid ($R_aR_g^{-1}$ = 47.7 to 100 ppm at 260 °C) with a significantly rapid response and recovery time, owing to its high specific surface area. Similarly, Geng *et al.* enhanced the acetic acid sensing properties by increasing the surface area and porosity of CuO.[101] The mesoporous CuO synthesized using a silica template showed a high response to acetic acid ($R_aR_g^{-1}$ = 27.2 to 100 ppm at 200 °C) with reversible sensing behavior.

4. Challenges and future perspectives

Various advances in chemoresistive gas sensors for food freshness monitoring have been achieved, resulting in the developments of sensors with high response, selectivity, rapid response/recovery behavior, and relatively small LOD. Nevertheless, chemoresistive gas sensors still face challenges such as water poisoning, power consumption, and low data accuracy. In this section, we present the primary challenges in optimizing chemoresistive gas sensors and propose possible solutions.

4.1. Water poisoning

Water poisoning deteriorates the performance of chemoresistive gas sensors as H_2O interacts with active sensing sites, resulting in the formation of hydroxyls on the surface of sensing materials. This hinders the formation of surface adsorbed oxygen species and/or adsorption of target molecules, leading to reduced gas sensing properties such as a decrease in response and change in resistance. Given that water vapor is a prevalent interferent in food freshness monitoring systems, achieving humidity-independent properties in gas sensors is important. Applying water-resistant layers on the sensing materials, inhibiting the penetrations of H_2O while enabling O_2 permeation, can be a viable solution to suppress water poisoning. For instance, Jeong *et al.* prepared a hydrophobic Tb_4O_7-coated In_2O_3 gas sensor to detect acetone without humidity dependence (Fig. 8a).[124] The Tb_4O_7 overlayer blocked the water and prevented the formation of hydroxyl groups on the surface of sensing materials. This humidity resistance layer was also successfully applied to diverse materials including SnO_2, ZnO, and Pd/SnO_2, confirming the general validity of Tb_4O_7 as a water-blocking layer. This phenomenon is also observed in other hydrophobic materials such as PDMS[125] and ZIF-8.[126] In addition, additives such as Pd, Rh, Sb, NiO, CuO, CeO_2, and Pr could be employed for suppressing humidity-dependent characteristics as they could capture or remove hydroxyls.[127–132] For examples, Yoon *et al.* proposed the underlying mechanism of CeO_2 to remove the humidity effect on sensing performance (Fig. 8b).[133] Upon exposure to water vapor, Ce^{4+} ions reduces to Ce^{3+}, and hydrogen ions (H^+) are generated. These chemical species react with hydroxyl groups on the In_2O_3 surface, regenerating the Ce^{4+} species and water vapor molecule. This phenomenon, called a hydroxyl scavenging reaction, gives humidity-independence to the sensing materials. Accordingly, designing appropriate heterojunctions between sensing materials and water-resistant components can be further explored for achieving humidity-resistant properties.

4.2. Power consumption

In general, chemoresistive gas sensors require thermal activation to generate charge carriers and enhance the number of surface oxygen species. Therefore, an external heater is necessary to ensure a consistent temperature of sensors for an extended period, even in varying atmospheric conditions. Thus, the power consumption of the sensor system should be considered for its practical use in real-time applications. These limitations regarding high power consumption can be solved by fabricating MEMS based gas sensors. The chemoresistive gas sensors with MEMS technology are composed of sensing materials and a heater in a single chip, which have advantages in miniaturization and small operating power.[134–136] For instance, Santra *et al.* utilized complementary metal oxide semiconductor (CMOS) MEMS to chemoresistive gas sensors to reduce power consumption of ZnO based ethanol sensor (Fig. 8c).[137] The CMOS MEMS showed a high thermal efficiency of 8.2 °C mW^{-1}, resulting in only 42.7 mW to heat up to 350 °C. Therefore, MEMS-based sensors can pave a new way for IoT application of food freshness monitoring. Furthermore, as an alternative to heaters, the utilizing of light sources such as light-emitting diodes (LEDs) can be suggested as another solution to enhance the material stability and lower operating power. A

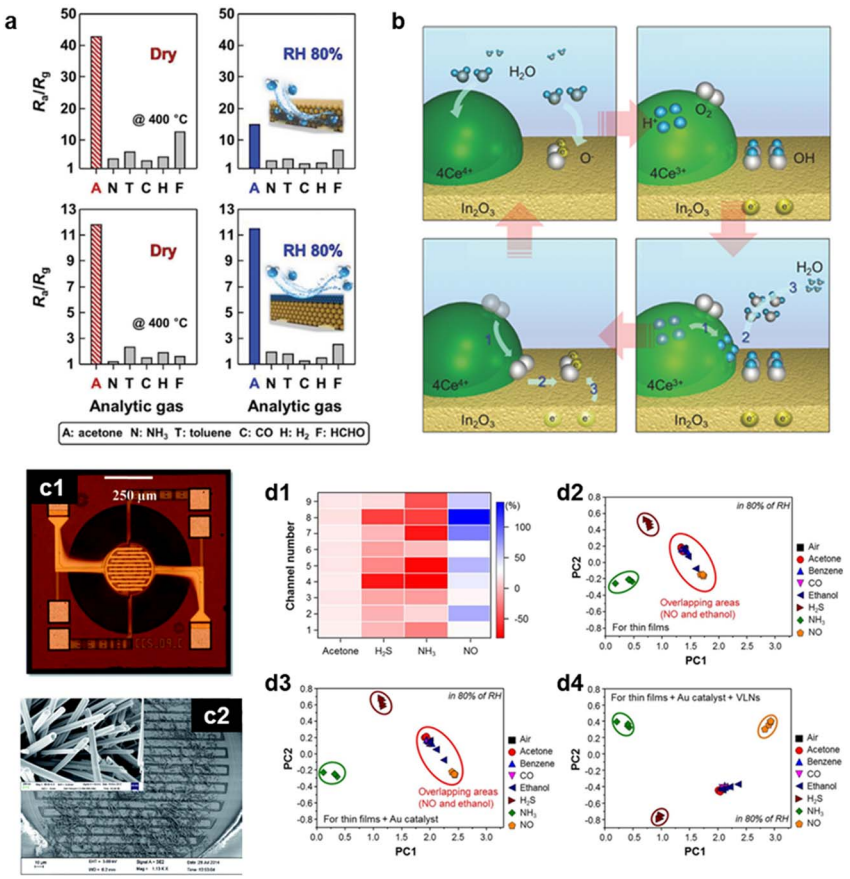

Fig. 8 (a) Gas response ($R_aR_g^{-1}$) of the pure In_2O_3 (upper) and the Tb_4O_7 coated In_2O_3 (lower) sensors exposed to 10 ppm analyte gases in dry and 80% RH conditions. Reproduced with permission.[124] Copyright 2020, Wiley. (b) Illustrations showing the fundamental mechanisms behind the humidity-independent properties of a CeO_2 coated In_2O_3 sensor. Reproduced with permission.[133] Copyright 2016, Wiley. (c1) Optical microscope image of CMOS MEMS, (c2) SEM image of the MEMS based ZnO sensor. Reproduced with permission.[137] Copyright 2015, The Royal Society of Chemistry. (d1) Color-mapped responses of sensor array to H_2S, NH_3, acetone and NO. PCA plots of (d2) thin films, (d3) Au functionalized thin films, (d4) Au functionalized villi-like structured thin films with PC1 and PC2 using responses of 8 different analyte gases in 80% RH conditions. Reproduced with permission.[146] Copyright 2016, American Chemical Society.

light source with a higher energy than the bandgap of the materials can generate the charge carriers and increase the conductivity at RT. This activation not only enhances the sensor response, but also improves the response and recovery kinetics.[138,139] Various strategies were reported to optimize the light activation effect including nanostructure design, heterojunction formation, and localized surface plasmon resonance.[140–142] Also, integration of the sensor platform with micro-LEDs can further enhance the sensor performance by reducing the distance between the light source and sensing materials.[143–145] Likewise, a light-activated gas sensor platform can be suggested as a rational strategy for the use of chemoresistive gas sensors in food quality monitoring.

4.3. Sensor accuracy and reliability

The low reliability of chemoresistive sensor, accompanied by the difficulty in discriminating target gas over other interferents, should be improved for its practical use for real-time freshness monitoring applications. The integration of several sensors possessing different sensing properties and applying pattern recognition enables the precise discrimination of the mixture gases in real situations. For example, Moon *et al.* integrated nine different sensors by fabricating 3 × 3 sensor arrays and measured the responses of sensors toward eight different analytic gases (CH_3COCH_3, C_6H_6, CO, C_2H_5OH, H_2S, NH_3, and NO; Fig. 8d).[146] They mapped the response amplitudes on a color scale and further investigated the data based on the principal component analysis (PCA). The sensor arrays showed the high selectivity toward H_2S, NH_3, and NO, implying that using multiple sensors is advantageous in precise discrimination of gases. Similarly, Jeong *et al.* discriminated between aromatic and nonaromatic gases by using a nine sensor array and PCA.[147] Notably, this sensor array not only differentiated aromatic and nonaromatic gases, but also quantitatively identified aromatic gases.

Additionally, utilizing machine learning to chemoresistive gas sensors could increase the reliability of sensor arrays by analyzing the response signals with sensitivity, and response/recovery speed at different temperatures and concentrations. For instance, Schroeder *et al.* fabricated twenty CNT-based chemical sensor arrays to discriminate the odor of cheese, liquor, and edible oil.[148] Through the investigation of gas

sensing transient data using two different models followed by training and testing, the proposed model classified samples of several foods with up to 91% accuracy. Moreover, Oh *et al.* successfully discriminated five different indoor air pollutants (C_6H_6, C_8H_{10}, C_7H_8, HCHO, and C_2H_5OH) under varied temperature and humid conditions by adopting machine learning to In_2O_3 based sensor array.[149] Overall, applying sensor array and machine learning to food quality monitoring applications is expected as a breakthrough in the reliability problem.

5. Conclusions

Chemoresistive gas sensors have emerged as a promising tool for real-time freshness monitoring, addressing the growing demands of the food industry. In this review, we have summarized the recent progress and future perspectives regarding chemoresistive sensors for monitoring food freshness. The detection of representative food quality marker gases, including C_2H_4, NH_3, C_3H_9N, and H_2S, has been achieved using metal oxides, carbon-based materials, TMDs, and other emerging materials. The selective detection of target gases, even in the presence of interferences, was achieved through the design of sensing materials with distinct chemical affinities or catalytic effects for specific gases. Therefore, designing sensing materials with desired chemical properties appears to be a promising strategy for real-time food freshness assessments. Nevertheless, challenges and limitations remain in the field of chemoresistive gas sensors, such as humidity-dependency, power consumption, and a lack of reliability. Thus, we have also described recent attempts to develop high-performance sensors by designing sensing materials and utilizing new technologies. Moreover, employing sensor arrays and machine learning based signal processing in gas analysis enables the selective discrimination between food quality marker gases. The development of diverse chemoresistive gas sensors with the adoption of innovative technologies will open up a new avenue in a wide range of agricultural and food packaging applications.

Author contributions

Seon Ju Park: investigation, visualization, original draft preparation. Soo Min Lee: investigation, visualization, original draft preparation. Mi-Hwa Oh: writing – reviewing and editing, funding acquisition. Yoon Suk Huh: writing – reviewing and editing, funding acquisition. Ho Won Jang: supervision, writing – reviewing and editing, supervision.

Conflicts of interest

There are no conflicts to declare.

Acknowledgements

This research was financially supported by Cooperative Research Program for Agriculture Science and Technology Development (Project No. PJ017067022022) Rural Development Administration, Republic of Korea. This work also supported by Nano Material Technology Development Program (2022M3H4A1A01011993) through NRF (National Research Foundation of Korea), funded by the Ministry of Science and ICT, Republic of Korea.

Notes and references

1 M. Alizadeh-Sani, E. Mohammadian, J.-W. Rhim and S. M. Jafari, *Trends Food Sci. Technol.*, 2020, **105**, 93–144.
2 B. Kuswandi, N. P. Asih, D. K. Pratoko, N. Kristiningrum and M. Moradi, *Packag. Technol. Sci.*, 2020, **33**, 321–332.
3 E. Balbinot-Alfaro, D. V. Craveiro, K. O. Lima, H. L. G. Costa, D. R. Lopes and C. Prentice, *Food Eng. Rev.*, 2019, **11**, 235–244.
4 C. Medina-Jaramillo, O. Ochoa-Yepes, C. Bernal and L. Famá, *Carbohydr. Polym.*, 2017, **176**, 187–194.
5 Y. Yano, M. Numata, H. Hachiya, S. Ito, T. Masadome, S. Ohkubo, Y. Asano and T. Imato, *Talanta*, 2001, **54**, 255–262.
6 G. Pampoukis, A. E. Lytou, A. A. Argyri, E. Z. Panagou and G.-J. E. Nychas, *Sensors*, 2022, **22**, 2800.
7 R. S. Andre, L. A. Mercante, M. H. Facure, R. C. Sanfelice, L. Fugikawa-Santos, T. M. Swager and D. S. Correa, *ACS Sens.*, 2022, **7**, 2104–2131.
8 S. P. Burg and E. A. Burg, *Science*, 1965, **148**, 1190–1196.
9 S. Y. Jeong, J. S. Kim and J. H. Lee, *Adv. Mater.*, 2020, **32**, 2002075.
10 S. Y. Park, Y. Kim, T. Kim, T. H. Eom, S. Y. Kim and H. W. Jang, *InfoMat*, 2019, **1**, 289–316.
11 S. Lee, S. Kim, G. B. Nam, T. H. Eom and H. W. Jang, *J. Semicond. Technol. Sci.*, 2022, **22**, 244–258.
12 N. Yamazoe, G. Sakai and K. Shimanoe, *Catal. Surv. Asia*, 2003, **7**, 63–75.
13 S.-J. Choi and I.-D. Kim, *Electron. Mater. Lett.*, 2018, **14**, 221–260.
14 Y. K. Jo, S.-Y. Jeong, Y. K. Moon, Y.-M. Jo, J.-W. Yoon and J.-H. Lee, *Nat. Commun.*, 2021, **12**, 1–9.
15 S. M. Lee, Y. K. Moon, K. Lim, S.-W. Park, S. J. Park, T.-H. Kim, S. Y. Kim, J.-H. Lee and Y.-M. Jo, *Sens. Actuators, B*, 2023, **382**, 133494.
16 Y. G. Song, J. Y. Park, J. M. Suh, Y.-S. Shim, S. Y. Yi, H. W. Jang, S. Kim, J. M. Yuk, B.-K. Ju and C.-Y. Kang, *Chem. Mater.*, 2018, **31**, 207–215.
17 S. J. Park, Y. K. Moon, S.-W. Park, S. M. Lee, T.-H. Kim, S. Y. Kim, J.-H. Lee and Y.-M. Jo, *ACS Appl. Mater. Interfaces*, 2023, **15**, 7102–7111.
18 J.-M. Jeon, Y.-S. Shim, S. D. Han, Y. H. Kim, C.-Y. Kang, J.-S. Kim, M. Kim and H. W. Jang, *J. Mater. Chem. A*, 2015, **3**, 17939–17945.
19 Y. Wang, J. Liu, X. Cui, Y. Gao, J. Ma, Y. Sun, P. Sun, F. Liu, X. Liang and T. Zhang, *Sens. Actuators, B*, 2017, **238**, 473–481.
20 J. Xu, X. Wang and J. Shen, *Sens. Actuators, B*, 2006, **115**, 642–646.
21 L. Wang, Z. Lou, R. Wang, T. Fei and T. Zhang, *Sens. Actuators, B*, 2012, **171**, 1180–1185.
22 E. Llobet, *Sens. Actuators, B*, 2013, **179**, 32–45.

23 Y. H. Kim, S. J. Kim, Y.-J. Kim, Y.-S. Shim, S. Y. Kim, B. H. Hong and H. W. Jang, *ACS Nano*, 2015, **9**, 10453–10460.
24 D. R. Kauffman and A. Star, *Angew. Chem., Int. Ed.*, 2008, **47**, 6550–6570.
25 Y. H. Kim, J. S. Park, Y.-R. Choi, S. Y. Park, S. Y. Lee, W. Sohn, Y.-S. Shim, J.-H. Lee, C. R. Park and Y. S. Choi, *J. Mater. Chem. A*, 2017, **5**, 19116–19125.
26 E. Singh, M. Meyyappan and H. S. Nalwa, *ACS Appl. Mater. Interfaces*, 2017, **9**, 34544–34586.
27 C. W. Lee, S. E. Jun, S. J. Kim, T. H. Lee, S. A. Lee, J. W. Yang, J. H. Cho, S. Choi, C. j. Kim and S. Y. Kim, *InfoMat*, 2023, e12427.
28 J. M. Suh, T. H. Lee, K. Hong, Y. G. Song, S. H. Cho, C.-Y. Kang, Y.-S. Shim, D. Lee, K. C. Kwon and H. W. Jang, *Sens. Actuators, B*, 2022, **369**, 132319.
29 E. Lee, Y. S. Yoon and D.-J. Kim, *ACS Sens.*, 2018, **3**, 2045–2060.
30 Y. Hu, W. Zheng, S. Fan, J. Zhang and X. Liu, *Appl. Phys. Rev.*, 2023, 10.
31 R. Kumar, W. Zheng, X. Liu, J. Zhang and M. Kumar, *Adv. Mater. Technol.*, 2020, **5**, 1901062.
32 C. W. Lee, T. H. Eom, S. H. Cho and H. W. Jang, *Adv. Sens. Res.*, 2023, 2200057.
33 X. Liu, T. Ma, N. Pinna and J. Zhang, *Adv. Funct. Mater.*, 2017, **27**, 1702168.
34 H. Furukawa, K. E. Cordova, M. O'Keeffe and O. M. Yaghi, *Science*, 2013, **341**, 1230444.
35 H.-C. Zhou, J. R. Long and O. M. Yaghi, *Chem. Rev.*, 2012, **112**, 673–674.
36 M. K. Lee, M. Shokouhimehr, S. Y. Kim and H. W. Jang, *Adv. Energy Mater.*, 2022, **12**, 2003990.
37 Y. M. Jo, Y. K. Jo, J. H. Lee, H. W. Jang, I. S. Hwang and D. J. Yoo, *Adv. Mater.*, 2022, 2206842.
38 W.-T. Koo, J.-S. Jang and I.-D. Kim, *Chem*, 2019, **5**, 1938–1963.
39 Y. Sun, B. Wang, Y. Hou, K. Suematsu, Z. Zhao, W. Zhang, K. Shimanoe and J. Hu, *J. Chem. Eng.*, 2023, **465**, 142818.
40 M. G. Campbell, S. F. Liu, T. M. Swager and M. Dinca, *J. Am. Chem. Soc.*, 2015, **137**, 13780–13783.
41 Z. Meng, R. M. Stolz and K. A. Mirica, *J. Am. Chem. Soc.*, 2019, **141**, 11929–11937.
42 W. C. Ko, M.-S. Kim, Y. J. Kwon, J. Jeong, W. R. Kim, H. Choi, J. K. Park and Y. K. Jeong, *J. Mater. Chem. A*, 2020, **8**, 19246–19253.
43 E. Lee, A. VahidMohammadi, Y. S. Yoon, M. Beidaghi and D.-J. Kim, *ACS Sens.*, 2019, **4**, 1603–1611.
44 S. J. Kim, H.-J. Koh, C. E. Ren, O. Kwon, K. Maleski, S.-Y. Cho, B. Anasori, C.-K. Kim, Y.-K. Choi and J. Kim, *ACS Nano*, 2018, **12**, 986–993.
45 W.-N. Zhao, N. Yun, Z.-H. Dai and Y.-F. Li, *RSC Adv.*, 2020, **10**, 1261–1270.
46 S. Sun, M. Wang, X. Chang, Y. Jiang, D. Zhang, D. Wang, Y. Zhang and Y. Lei, *Sens. Actuators, B*, 2020, **304**, 127274.
47 M. Liu, Z. Wang, P. Song, Z. Yang and Q. Wang, *Sens. Actuators, B*, 2021, **340**, 129946.
48 Y.-J. Chen, Y.-Y. Wen, W.-H. Li, Z.-H. Fu, G.-E. Wang and G. Xu, *Nano Lett.*, 2023, **23**, 3614–3622.
49 L. Zhou, Y. Hu, S. Li, X. Liu and J. Zhang, *Appl. Phys. Lett.*, 2023, 123.
50 D. H. Kim, Y.-S. Shim, J.-M. Jeon, H. Y. Jeong, S. S. Park, Y.-W. Kim, J.-S. Kim, J.-H. Lee and H. W. Jang, *ACS Appl. Mater. Interfaces*, 2014, **6**, 14779–14784.
51 Y.-M. Jo, T.-H. Kim, C.-S. Lee, K. Lim, C. W. Na, F. Abdel-Hady, A. A. Wazzan and J.-H. Lee, *ACS Appl. Mater. Interfaces*, 2018, **10**, 8860–8868.
52 K. J. Choi and H. W. Jang, *Sensors*, 2010, **10**, 4083–4099.
53 J. M. Suh, K. C. Kwon, T. H. Lee, C. Kim, C. W. Lee, Y. G. Song, M.-J. Choi, S. Choi, S. H. Cho and S. Kim, *Sens. Actuators, B*, 2021, **333**, 129566.
54 H. G. Moon, Y.-S. Shim, H. W. Jang, J.-S. Kim, K. J. Choi, C.-Y. Kang, J.-W. Choi, H.-H. Park and S.-J. Yoon, *Sens. Actuators, B*, 2010, **149**, 116–121.
55 J.-H. Lee, *Sens. Actuators, B*, 2009, **140**, 319–336.
56 L. Zhou, Z. Li, X. Chang, X. Liu, Y. Hu, M. Li, P. Xu, N. Pinna and J. Zhang, *Small*, 2023, 2301485.
57 G. Lei, H. Pan, H. Mei, X. Liu, G. Lu, C. Lou, Z. Li and J. Zhang, *Chem. Soc. Rev.*, 2022, 7260–7280.
58 Y.-S. Shim, H. G. Moon, L. Zhang, S.-J. Yoon, Y. S. Yoon, C.-Y. Kang and H. W. Jang, *RSC Adv.*, 2013, **3**, 10452–10459.
59 J. M. Suh, Y. S. Shim, D. H. Kim, W. Sohn, Y. Jung, S. Y. Lee, S. Choi, Y. H. Kim, J. M. Jeon and K. Hong, *Adv. Mater. Technol.*, 2017, **2**, 1600259.
60 X. Kou, N. Xie, F. Chen, T. Wang, L. Guo, C. Wang, Q. Wang, J. Ma, Y. Sun and H. Zhang, *Sens. Actuators, B*, 2018, **256**, 861–869.
61 C.-S. Lee, Z. Dai, H.-Y. Li, Y.-M. Jo, B.-Y. Kim, H.-G. Byun, I. Hwang and J.-H. Lee, *Sens. Actuators, B*, 2018, **273**, 1–8.
62 K.-I. Choi, H.-J. Kim, Y. C. Kang and J.-H. Lee, *Sens. Actuators, B*, 2014, **194**, 371–376.
63 K. Lim, Y.-M. Jo, S. Kim, J.-W. Yoon, S.-Y. Jeong, J.-S. Kim, H. J. Choi, Y. Cho, J. Park and Y. W. Jeong, *Sens. Actuators, B*, 2021, **348**, 130665.
64 R. Zhou, X. Lin, D. Xue, F. Zong, J. Zhang, X. Duan, Q. Li and T. Wang, *Sens. Actuators, B*, 2018, **260**, 900–907.
65 S. H. Kim, Y. K. Moon, J.-H. Lee, Y. C. Kang and S.-Y. Jeong, *J. Mater. Chem. A*, 2023, **11**, 1159–1169.
66 Y. K. Moon, S. Y. Jeong, Y. M. Jo, Y. K. Jo, Y. C. Kang and J. H. Lee, *Adv. Sci.*, 2021, **8**, 2004078.
67 Y. Y. Broza, X. Zhou, M. Yuan, D. Qu, Y. Zheng, R. Vishinkin, M. Khatib, W. Wu and H. Haick, *Chem. Rev.*, 2019, **119**, 11761–11817.
68 L. Capelli, S. Sironi and R. D. Rosso, *Sensors*, 2014, **14**, 19979–20007.
69 S. Y. Jeong, Y. K. Moon, T. H. Kim, S. W. Park, K. B. Kim, Y. C. Kang and J. H. Lee, *Adv. Sci.*, 2020, **7**, 1903093.
70 Y. K. Moon, J. H. Kim, S.-Y. Jeong, S. M. Lee, S. J. Park, T. H. Kim, J.-H. Lee and Y. C. Kang, *J. Mater. Chem. A*, 2023, **11**, 666–675.
71 B. Esser, J. M. Schnorr and T. M. Swager, *Angew. Chem., Int. Ed.*, 2012, **51**, 5752–5756.
72 Q. Zhao, Z. Duan, Z. Yuan, X. Li, W. Si, B. Liu, Y. Zhang, Y. Jiang and H. Tai, *Chin. Chem. Lett.*, 2020, **31**, 2045–2049.

73 L.-P. Wang, Z. Jin, T. Luo, Y. Ding, J.-H. Liu, X.-F. Wang and M.-Q. Li, *New J. Chem.*, 2019, **43**, 3619–3624.
74 T. Järvinen, G. S. Lorite, J. Peräntie, G. Toth, S. Saarakkala, V. K. Virtanen and K. Kordas, *Nanotechnol*, 2019, **30**, 405501.
75 K. Lee, R. Gatensby, N. McEvoy, T. Hallam and G. S. Duesberg, *Adv. Mater.*, 2013, **25**, 6699–6702.
76 T. Kim, T. H. Lee, S. Y. Park, T. H. Eom, I. Cho, Y. Kim, C. Kim, S. A. Lee, M.-J. Choi and J. M. Suh, *ACS Nano*, 2023, **17**, 4404–4413.
77 Z. Ma, P. Chen, W. Cheng, K. Yan, L. Pan, Y. Shi and G. Yu, *Nano Lett.*, 2018, **18**, 4570–4575.
78 A. T. Güntner, M. Wied, N. J. Pineau and S. E. Pratsinis, *Adv. Sci.*, 2020, **7**, 1903390.
79 D. Zhang, S. Yu, X. Wang, J. Huang, W. Pan, J. Zhang, B. E. Meteku and J. Zeng, *J. Harzard. Mater.*, 2022, **423**, 127160.
80 S. F. Liu, A. R. Petty, G. T. Sazama and T. M. Swager, *Angew. Chem., Int. Ed.*, 2015, **54**, 6554–6557.
81 Y. H. Cho, Y. C. Kang and J.-H. Lee, *Sens. Actuators, B*, 2013, **176**, 971–977.
82 P. Srinivasan and J. B. B. Rayappan, *Sens. Actuators, B*, 2021, **349**, 130759.
83 J.-S. Kim, K. B. Kim, H.-Y. Li, C. W. Na, K. Lim, Y. K. Moon, J. W. Yoon and J.-H. Lee, *J. Mater. Chem.*, 2021, **9**, 16359–16369.
84 Y. H. Cho, Y. N. Ko, Y. C. Kang, I.-D. Kim and J.-H. Lee, *Sens. Actuators, B*, 2014, **195**, 189–196.
85 W. Yan, H. Xu, M. Ling, S. Zhou, T. Qiu, Y. Deng, Z. Zhao and E. Zhang, *ACS Sens.*, 2021, **6**, 2613–2621.
86 T.-H. Kim, J.-W. Yoon, Y. C. Kang, F. Abdel-Hady, A. Wazzan and J.-H. Lee, *Sens. Actuators, B*, 2017, **240**, 1049–1057.
87 Q. Liu, S. Mukherjee, R. Huang, K. Liu, T. Liu, K. Liu, R. Miao, H. Peng and Y. Fang, *Chem.–Asian J.*, 2019, **14**, 2751–2758.
88 Y. Li, W. Luo, N. Qin, J. Dong, J. Wei, W. Li, S. Feng, J. Chen, J. Xu and A. A. Elzatahry, *Angew. Chem., Int. Ed.*, 2014, **53**, 9035–9040.
89 T. Wang, J. Liu, Y. Zhang, Q. Liang, R. Wu, H.-S. Tsai, Y. Wang and J. Hao, *J. Mater. Chem. A*, 2022, **10**, 4306–4315.
90 Y.-X. Jin, J. Chen, Y.-J. Chen, W.-H. Deng, X.-L. Ye, G.-E. Wang and G. Xu, *J. Mater. Chem. A*, 2023, **11**, 7179–7183.
91 O. Ovsianytskyi, Y.-S. Nam, O. Tsymbalenko, P.-T. Lan, M.-W. Moon and K.-B. Lee, *Sens. Actuators, B*, 2018, **257**, 278–285.
92 C. Z. Wang, J. Chen, Q. H. Li, G. E. Wang, X. L. Ye, J. Lv and G. Xu, *Angew. Chem., Int. Ed.*, 2023, **62**, e202302996.
93 T. Lee, J. O. Kim, C. Park, H. Kim, M. Kim, H. Park, I. Kim, J. Ko, K. Pak and S. Q. Choi, *Adv. Mater.*, 2022, **34**, 2107696.
94 X. Guo, Y. Ding, C. Liang, B. Du, C. Zhao, Y. Tan, Y. Shi, P. Zhang, X. Yang and Y. He, *Sens. Actuators, B*, 2022, **357**, 131424.
95 H. Fang, S. Li, W. Jiang, H. Zhao, C. Han, J. Li, G. Wang, Y. Zhang, S. Wang and J. Deng, *Sens. Actuators, B*, 2022, **368**, 132225.
96 Q. Zhou, L. Xu, Z. Kan, L. Yang, Z. Chang, B. Dong, X. Bai, G. Lu and H. Song, *J. Harzard. Mater.*, 2022, **426**, 128075.
97 Q. Zhou, L. Yang, Z. Kan, J. Lyu, M. X. Wang, B. Dong, X. Bai, Z. Chang, H. Song and L. Xu, *J. Chem. Eng.*, 2022, **450**, 138014.
98 K. Hagedorn, W. Li, Q. Liang, S. Dilger, M. Noebels, M. R. Wagner, J. S. Reparaz, A. Dollinger, J. Schmedt auf der Günne and T. Dekorsy, *Adv. Funct. Mater.*, 2016, **26**, 3424–3437.
99 C. Li, Y. Liu, W. Wan, Y. Li, Y. Ma, J. Zhang, X. Ren and H. Zhao, *Sens. Actuators, B*, 2020, **318**, 128209.
100 W. Jin, S. Ma, Z. Tie, W. Li, J. Luo, L. Cheng, X. Xu, T. Wang, X. Jiang and Y. Mao, *Appl. Surf. Sci.*, 2015, **353**, 71–78.
101 W. Geng, Z. Ma, J. Yang, L. Duan, F. Li and Q. Zhang, *Sens. Actuators, B*, 2021, **334**, 129639.
102 V. Shumeiko, E. Malach, Y. Helman, Y. Paltiel, G. Bisker, Z. Hayouka and O. Shoseyov, *Sens. Actuators, B*, 2021, **327**, 128832.
103 N. Keller, M.-N. Ducamp, D. Robert and V. Keller, *Chem. Rev.*, 2013, **113**, 5029–5070.
104 M. E. Saltveit, *Postharvest Biol. Technol.*, 1999, **15**, 279–292.
105 K.-H. Kim, R. Pal, J.-W. Ahn and Y.-H. Kim, *Waste Manage.*, 2009, **29**, 1265–1273.
106 C.-C. Zhao and J.-B. Eun, *J. Food Sci. Technol.*, 2018, **55**, 5082–5090.
107 X. Liu, W. Zheng, R. Kumar, M. Kumar and J. Zhang, *Coord. Chem. Rev.*, 2022, **462**, 214517.
108 L. Gram and H. H. Huss, *Int. J. Food Microbiol.*, 1996, **33**, 121–137.
109 G. Moula, M. Bose and S. Sarkar, *Inorg. Chem.*, 2013, **52**, 5316–5327.
110 J. Sujiwo, D. Kim and A. Jang, *Poult. Sci.*, 2018, **97**, 2887–2894.
111 A. E.-D. A. Bekhit, B. W. Holman, S. G. Giteru and D. L. Hopkins, *Trends Food Sci. Technol.*, 2021, **109**, 280–302.
112 G. Esposito, S. Sciuto and P. L. Acutis, *Food Control*, 2018, **94**, 162–166.
113 C. C. Balamatsia, A. Patsias, M. G. Kontominas and I. N. Savvaidis, *Food Chem.*, 2007, **104**, 1622–1628.
114 K. Mitsubayashi, Y. Kubotera, K. Yano, Y. Hashimoto, T. Kon, S. Nakakura, Y. Nishi and H. Endo, *Sens. Actuators, B*, 2004, **103**, 463–467.
115 N. C. Jeong, J. S. Lee, E. L. Tae, Y. J. Lee and K. B. Yoon, *Angew. Chem., Int. Ed.*, 2008, **47**, 10128–10132.
116 D. Dave and A. E. Ghaly, *Am. J. Agric. Biol. Sci.*, 2011, **6**, 486–510.
117 P. Dalgaard, L. Gram and H. H. Huss, *Int. J. Food Microbiol.*, 1993, **19**, 283–294.
118 H. Li, W. Geng, X. Sun, W. Wei, X. Mu, W. Ahmad, M. M. Hassan, Q. Ouyang and Q. Chen, *Meat Sci.*, 2021, **177**, 108507.
119 D. B. Rodriguez, H. A. Frank and H. Y. Yamamoto, *J. Sci. Food Agric.*, 1969, **20**, 15–17.
120 G. Kim, B.-K. Cho, S. H. Oh and K.-B. Kim, *J. Biosyst. Eng.*, 2020, **45**, 261–271.

121 R. Pierami and K. Stevenson, *J. Dairy Sci.*, 1976, **59**, 1010–1015.
122 E. J. Bartowsky, *Lett. Appl. Microbiol.*, 2009, **48**, 149–156.
123 E. J. Bartowsky and P. A. Henschke, *Int. J. Food Microbiol.*, 2008, **125**, 60–70.
124 S. Y. Jeong, Y. K. Moon, J. K. Kim, S. W. Park, Y. K. Jo, Y. C. Kang and J. H. Lee, *Adv. Funct. Mater.*, 2021, **31**, 2007895.
125 F. Qu, S. Zhang, C. Huang, X. Guo, Y. Zhu, T. Thomas, H. Guo, J. P. Attfield and M. Yang, *Angew. Chem., Int. Ed.*, 2021, **60**, 6561–6566.
126 G. S. Kim, Y. Lim, J. Shin, J. Yim, S. Hur, H. C. Song, S. H. Baek, S. K. Kim, J. Kim and C. Y. Kang, *Adv. Sci.*, 2023, 2301002.
127 N. Ma, K. Suematsu, M. Yuasa, T. Kida and K. Shimanoe, *ACS Appl. Mater. Interfaces*, 2015, **7**, 5863–5869.
128 K.-I. Choi, S.-J. Hwang, Z. Dai, Y. C. Kang and J.-H. Lee, *RSC Adv.*, 2014, **4**, 53130–53136.
129 K. Suematsu, M. Sasaki, N. Ma, M. Yuasa and K. Shimanoe, *ACS Sens.*, 2016, **1**, 913–920.
130 H. R. Kim, A. Haensch, I. D. Kim, N. Barsan, U. Weimar and J. H. Lee, *Adv. Funct. Mater.*, 2011, **21**, 4456–4463.
131 Y. Sun, Z. Zhao, K. Suematsu, P. Li, Z. Yu, W. Zhang, J. Hu and K. Shimanoe, *ACS Sens.*, 2020, **5**, 1040–1049.
132 J.-S. Kim, C. W. Na, C.-H. Kwak, H.-Y. Li, J. W. Yoon, J.-H. Kim, S.-Y. Jeong and J.-H. Lee, *ACS Appl. Mater. Interfaces*, 2019, **11**, 25322–25329.
133 J. W. Yoon, J. S. Kim, T. H. Kim, Y. J. Hong, Y. C. Kang and J. H. Lee, *Small*, 2016, **12**, 4229–4240.
134 Q. Zhou, A. Sussman, J. Chang, J. Dong, A. Zettl and W. Mickelson, *Sens. Actuators, A*, 2015, **223**, 67–75.
135 L. Xiao, S. Xu, G. Yu and S. Liu, *Sens. Actuators, B*, 2018, **255**, 2002–2010.
136 N. Luo, C. Wang, D. Zhang, M. Guo, X. Wang, Z. Cheng and J. Xu, *Sens. Actuators, B*, 2022, **354**, 130982.
137 S. Santra, A. De Luca, S. Bhaumik, S. Ali, F. Udrea, J. Gardner, S. Ray and P. Guha, *RSC Adv.*, 2015, **5**, 47609–47616.
138 T. H. Eom, S. H. Cho, J. M. Suh, T. Kim, T. H. Lee, S. E. Jun, J. W. Yang, J. Lee, S.-H. Hong and H. W. Jang, *J. Mater. Chem. A*, 2021, **9**, 11168–11178.
139 T. H. Eom, S. H. Cho, J. M. Suh, T. Kim, J. W. Yang, T. H. Lee, S. E. Jun, S. J. Kim, J. Lee and S. H. Hong, *Small*, 2022, **18**, 2106613.
140 D. Cho, J. M. Suh, S. H. Nam, S. Y. Park, M. Park, T. H. Lee, K. S. Choi, J. Lee, C. Ahn and H. W. Jang, *Adv. Sci.*, 2021, **8**, 2001883.
141 Y.-M. Jo, K. Lim, J. W. Yoon, Y. K. Jo, Y. K. Moon, H. W. Jang and J.-H. Lee, *ACS Cent. Sci.*, 2021, **7**, 1176–1182.
142 K. Lim, Y. M. Jo, J. W. Yoon, J. S. Kim, D. J. Lee, Y. K. Moon, J. W. Yoon, J. H. Kim, H. J. Choi and J. H. Lee, *Small*, 2021, **17**, 2100438.
143 J. M. Suh, T. H. Eom, S. H. Cho, T. Kim and H. W. Jang, *Mater. Adv.*, 2021, **2**, 827–844.
144 O. Casals, N. Markiewicz, C. Fabrega, I. Gràcia, C. Cané, H. S. Wasisto, A. Waag and J. D. Prades, *ACS Sens.*, 2019, **4**, 822–826.
145 J. E. Ryu, S. Park, Y. Park, S. W. Ryu, K. Hwang and H. W. Jang, *Adv. Mater.*, 2022, 2204947.
146 H. G. Moon, Y. Jung, S. D. Han, Y.-S. Shim, B. Shin, T. Lee, J.-S. Kim, S. Lee, S. C. Jun and H.-H. Park, *ACS Appl. Mater. Interfaces*, 2016, **8**, 20969–20976.
147 S.-Y. Jeong, Y. K. Moon, J. Wang and J.-H. Lee, *Nat. Commun.*, 2023, **14**, 233.
148 V. Schroeder, E. D. Evans, Y.-C. M. Wu, C.-C. A. Voll, B. R. McDonald, S. Savagatrup and T. M. Swager, *ACS Sens.*, 2019, **4**, 2101–2108.
149 J. Oh, S. H. Kim, M.-J. Lee, H. Hwang, W. Ku, J. Lim, I.-S. Hwang, J.-H. Lee and J.-H. Hwang, *Sens. Actuators, B*, 2022, **364**, 131894.